Diffuse Reflectance Imaging with Astronomical Applications

Samuel W. Hasinoff
TTIC

Anat Levin
Weizmann Institute

Philip R. Goode
Big Bear Solar Observatory

William T. Freeman
MIT CSAIL

Abstract

Diffuse objects generally tell us little about the surrounding lighting, since the radiance they reflect blurs together incident lighting from many directions. In this paper we discuss how occlusion geometry *can help invert diffuse reflectance to recover lighting or surface albedo. Self-occlusion in the scene can be regarded as a form of coding, creating high frequencies that improve the conditioning of diffuse light transport. Our analysis builds on a basic observation that diffuse reflectors with sufficiently detailed geometry can fully resolve the incident lighting. Using a Bayesian framework, we propose a novel reconstruction method based on high-resolution photography, taking advantage of visibility changes near occlusion boundaries. We also explore the limits of single-pixel observations as the diffuse reflector (and potentially the lighting) vary over time. Diffuse reflectance imaging is particularly relevant for astronomy applications, where diffuse reflectors arise naturally but the incident lighting and camera position cannot be controlled. To test our approaches, we first study the feasibility of using the moon as a diffuse reflector to observe the earth as seen from space. Next we present a reconstruction of Mars using historical photometry measurements not previously used for this purpose. As our results suggest, diffuse reflectance imaging expands our notion of what can qualify as a camera.*

1. Introduction

Diffuse objects like ping pong balls generally provide us with little information about the surrounding lighting, since the radiance they reflect blurs together incident lighting from many directions. Whereas mirrored surfaces in the scene can effectively be treated as new cameras [12], light reflected from diffuse objects is far more difficult to interpret. In this paper we present a detailed investigation of how *occlusion geometry* can help us resolve more detailed structure using the reflectance from diffuse objects, to recover the incident lighting or the surface albedo.

The starting point for our analysis is the observation that with sufficiently detailed known scene geometry, even diffuse scenes can resolve the incident lighting to arbitrary fidelity, limited only by diffraction. The key benefit of occlusion geometry is its ability to introduce high frequencies into our measurements, which correspond to projections of the incoming lighting. Using a Bayesian framework, we propose a new reconstruction method based on high-resolution photography, taking advantage of the rapid visibility changes near occlusion boundaries. We also explore the limits of single-pixel observations, taking into account the challenging case where both the reflector and lighting are time-varying.

In reflectance imaging, the reflectors themselves can be thought of as part of the larger imaging system. Described in these terms, the occlusion geometry can be interpreted as a form of visibility coding, analogous to the amplitude masks used in computational photography [29, 10]. This coding has the general effect of improving the conditioning of light transport, and can help us resolve more structure from diffuse reflectors. Though we may sometimes have the opportunity to introduce such coding deliberately, via control of the scene geometry, it may also arise naturally from geometric complexity or variations over time.

Diffuse reflectance imaging is closely related to previous work on inverse rendering [1, 16, 17, 18], however our emphasis on occlusion geometry means that we are not subject to the same theoretical limits associated with convex Lambertian objects [1, 16, 18]. Our approach is also related to more general light transport analysis [21, 22], however the astronomy applications we consider do not let us control the incident lighting. One of our applications, reconstructing the surface of distant planets, is a classic problem in astronomy [20, 26, 28], however, we are the first to adopt a Bayesian analysis, which also helps us generalize to the situation where the unknown lighting is time-varying as well.

Our paper offers four main contributions over the state of the art. First, we show that diffuse light transport is theoretically invertible, given sufficiently complex scene geometry. Second, we present a Bayesian method to invert light transport, able to handle unknown time-varying lighting. Third, we introduce a new method for diffuse reflectance imaging, based on analyzing variations near occlusion boundaries in a single high-resolution shot. Fourth, we validate our proposed methods using several astronomy applications, demonstrating through simulation the feasibility of reconstructing the earth from its reflection in the moon, and recovering the surface of Mars from single-pixel measurements.

2. Theory of Shadowed Reflectance Imaging

Our description of diffuse reflectance follows a basic single-bounce model of light transport where light reflects from opaque scene objects according to their BRDF, but without further inter-reflections [1, 16, 17, 18]. Under this model we can express the measured light field using a simplified version of the rendering equation,

$$B(\mathbf{p}, \vec{\omega}_o) = \int_\Omega \alpha(\mathbf{p})\, L(\mathbf{p}, \vec{\omega}_i)\, \rho(\vec{\omega}_i, \vec{\omega}_o)\, V(\mathbf{p}, \vec{\omega}_i)\, \max(\vec{\omega}_i \cdot \vec{n}, 0)\, \mathrm{d}\vec{\omega}_i \;, \quad (1)$$

integrating over the hemisphere of incident lighting directions for a given surface point $\mathbf{p}$ with normal $\vec{n}$. The integrand is the product of four main terms: the surface albedo $\alpha(\mathbf{p})$; the incoming radiance $L(\mathbf{p}, \vec{\omega}_i)$, which describes the lighting environment; the BRDF $\rho(\vec{\omega}_i, \vec{\omega}_o)$, which defines reflectance; and a binary visibility mask $V(\mathbf{p}, \vec{\omega}_i)$, which encodes self-occlusion. As noted in previous work, this integral can be interpreted as convolution of the BRDF and the lighting. For a distant lighting and a smooth and convex object, this analogy is exact and light transport may be written as convolution in a spherical basis [1, 16, 17].

As in previous inverse rendering methods that seek the incident lighting from diffuse reflectance, we restrict ourselves to distant illumination, $L(\mathbf{p}, \vec{\omega}_i) = L(\vec{\omega}_i)$ [1, 16, 17, 18]. Unlike these methods, we do not introduce further restrictions limiting ourselves to Lambertian surfaces [1, 16] or to smooth and convex objects [1, 16, 18].

To make the subsequent discussion concrete, we focus on the case where geometry and albedo are known and we seek to recover the unknown lighting. Similar analysis applies when lighting is known and we seek to reconstruct the surface albedo instead. Our applications cover both unknown lighting (Secs. 3.1 and 4.1) and unknown albedo (Sec. 4.2).

Shadowed reflectance The main feature distinguishing our analysis from previous work is its closer attention to shadowing effects [17, 4], where occlusion geometry may block portions of the incoming lighting.

Recovering the lighting from diffuse reflection is considered to be particularly challenging for smooth objects. According to the well-known theory, images of a convex Lambertian object over all distant lighting conditions lie very close to a rank-9 subspace [1, 16]. As this result implies, no more than 9 basis coefficients describing the incident lighting can generally be recovered from images of arbitrary convex Lambertian objects.

Our focus on occlusion geometry extends the capabilities of inverse rendering, providing a more optimistic view of what structure may be recovered from diffuse scenes, provided that the scene geometry is known to high accuracy. The reconstruction methods we describe rely almost exclusively on occlusion geometry to improve the conditioning of light transport, based on two sources of occlusion: self-occlusion due to geometric complexity, and visibility at occluding contours. The relationship between geometric complexity and high frequencies in rendered images has long been studied in computer graphics [4]. For more general methods for inverting light transport, which rely on a brute-force measurement under many lighting conditions, occlusions in the scene are taken into account implicitly [21, 22].

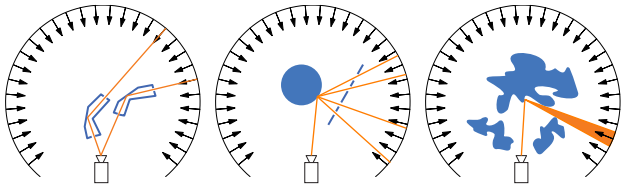

(a) double-pinhole scene units (b) coded reflectance imaging (c) natural geometric complexity

Figure 1: Sculpture design for diffuse reflectance imaging, using scene geometry (blue) to filter the incident lighting. In theory, by populating the scene with pinhole camera units (a), the lighting can be recovered to arbitrary fidelity, up to diffraction. A related approach involves a coded occluder (b) or objects with naturally complex geometry (c).

Matrix formulation In a discrete setting, the linearity of light transport lets express Eq. (1) in matrix form as $\mathbf{y} = \mathbf{A}\mathbf{x}$, relating observed image pixels $\mathbf{y}$ and the distant incident lighting $\mathbf{x}$ according to a transfer matrix $\mathbf{A}$ quantifying diffuse shadowed light transport. Each column of this matrix corresponds to an image when the scene is lit from a single direction with unit radiance. Each row corresponds to the lighting response for a particular pixel, modulated by the visibility of incident lighting directions. In general, the rank of this matrix is less than the lighting resolution (*i.e.*, some modes of $\mathbf{x}$ are not measurable), so we need some prior on the lighting to invert light transport in practice.

2.1. Sculpture Design for Reflectance Imaging

To explore the limits of reflectance imaging, we consider the problem of diffuse "sculpture design" (Fig. 1), where our task is to create a 3D shape from some volume of diffuse material, so that when the shape is introduced into the scene it will best let us resolve the incident lighting.

Although we pose this task mainly as a thought experiment, such an approach could potentially be useful for covert imaging applications, where objects with obvious imaging potential, such as mirrors, would be disallowed.

Pinhole scene design We make the basic observation that with the ability to control its shape arbitrarily, we can use the diffuse material to *manufacture* a camera out of scene geometry. In particular, we can populate the scene with a collection of camera units, each with two pinholes, oriented toward a particular camera ray and incident lighting direction respectively (Fig. 1a).

This extreme form of sculpture design embodies a pos-

itive theoretical result: with sufficiently detailed geometry we can resolve incident lighting to arbitrarily high frequency, up to the diffraction limit, independent of the BRDF of the scene. In our matrix formulation, the double-pinhole camera construction introduces per-row visibility masks that are zero everywhere except for one lighting direction.

Coded reflectance imaging In practice, our double-pinhole design would be difficult to manufacture, and the limited light-gathering ability of pinhole imaging would yield low SNR under a limited time budget. To address these problems, we consider several related designs.

By introducing a planar coded occluder into the scene, we generalize our previous result slightly. Points on the main object will thus reflect light from a discrete set lighting directions, rather than just one (Fig. 1b). Although inverting the light transport with a coded occluder is not as trivial as in the pinhole case, such a coded occlusion mask can help optimize SNR by trading off a blurrier reconstruction for relatively lower noise.

In fact, any sufficiently complex diffuse shape can possess natural self-occlusion properties sufficient to recover the incident lighting in well-conditioned way (Fig. 1c). For an unknown scene of this type, our first task is to recover the geometry or calibrate the corresponding light transport matrix directly [21, 22].

2.2. Reconstruction Methods

Bayesian linear estimation To invert the linear diffuse light transport operator, we adopt a standard Bayesian formulation [3], where the observations are subject to Gaussian noise, $\mathrm{p}(\mathbf{y}|\mathbf{x}) = \mathcal{N}\big(\mathbf{A}\mathbf{x}, \eta^2\mathbf{I}\big)$, and we define some prior distribution $\mathrm{p}(\mathbf{x})$ on the unknown lighting.

With a Gaussian prior of the form $\mathrm{p}(\mathbf{x}) = \mathcal{N}\big(\mathbf{0}, \mathbf{\Sigma_x}\big)$, for example, penalizing the sum of squared derivatives, we can derive a closed form for the posterior, $\mathrm{p}(\mathbf{x}|\mathbf{y}) = \mathcal{N}\big(\mathbf{\Sigma}(\frac{1}{\eta^2}\mathbf{A}^{\mathrm{T}}\mathbf{y}), \mathbf{\Sigma}\big)$, where $\mathbf{\Sigma} = (\mathbf{\Sigma_x}^{-1} + \frac{1}{\eta^2}\mathbf{A}^{\mathrm{T}}\mathbf{A})^{-1}$ [3, 10]. The mean of this distribution is the MAP estimate, which for a Gaussian prior is equivalent to classic Wiener filtering.

In our applications, we use a sparse derivative prior instead, penalizing the sum of derivatives transformed by the heavy-tailed function $g(z) = |z|^{0.8}$ [10]. This prior favors fewer but larger discontinuities in the lighting, better matching the statistics of natural images. While the MAP estimate corresponding to our sparse prior does not have a closed form, it may be computed iteratively using the iterative reweighted least squares algorithm.

Marginalizing out temporal variation For certain applications (see Sec. 4.1), the reconstruction problem is more challenging because the unknown lighting vector $\mathbf{x}$ we seek to reconstruct varies over time. In such cases, it is no longer straightforward to combine observations made at different times, even if we would be satisfied with reconstructing the time-averaged lighting. By modeling temporal lighting correlations explicitly, our Bayesian framework defines how to fully exploit all observations to reconstruct the lighting.

Our approach to time-varying lighting involves dividing the observations into temporal bins, $\mathbf{y}^{\mathrm{T}} = [\mathbf{y}_1{}^{\mathrm{T}} \cdots \mathbf{y}_D{}^{\mathrm{T}}]$. This division corresponds to assuming that observations within bins are generated with the same lighting, and that lighting across bins is uncorrelated. We express the lighting for the i-th bin as $\mathbf{x} + \mathbf{t}_i$, where $\mathbf{x}$ is the stable lighting component we wish to reconstruct, and $\mathbf{t}_i$ is the time-varying component. Accordingly, we have the observation model

$$\mathrm{p}(\mathbf{y}|\mathbf{x}, \mathbf{t}_1, \ldots, \mathbf{t}_D) = \mathcal{N}\Big(\begin{bmatrix}\mathbf{A}_1(\mathbf{x}+\mathbf{t}_1)\\ \vdots \\ \mathbf{A}_D(\mathbf{x}+\mathbf{t}_D)\end{bmatrix}, \eta^2\mathbf{I}\Big) \ . \quad (2)$$

By assuming that the time-varying components of the lighting are Gaussian, $\mathrm{p}(\mathbf{t}_i) = \mathcal{N}\big(\mathbf{0}, \mathbf{\Sigma_t}\big)$, we can marginalize out their influence. Using the independence of per-bin lighting variations $\mathbf{t}_i$ we derive an analytic expression for the likelihood of the stable lighting component,

$$\mathrm{p}(\mathbf{y}|\mathbf{x}) = \mathcal{N}\Big(\begin{bmatrix}\mathbf{A}_1\\ \vdots \\ \mathbf{A}_D\end{bmatrix}\mathbf{x}, \begin{bmatrix}\mathbf{A}_1\mathbf{\Sigma_t}\mathbf{A}_1{}^{\mathrm{T}} & & \mathbf{0}\\ & \ddots & \\ \mathbf{0} & & \mathbf{A}_D\mathbf{\Sigma_t}\mathbf{A}_D{}^{\mathrm{T}}\end{bmatrix} + \eta^2\mathbf{I}\Big) \, , \quad (3)$$

where the block-diagonal covariance structure effectively treats the time-varying lighting as correlated noise. From this point it is straightforward to compute the MAP estimate for $\mathbf{x}$ as before. For example, for a Gaussian prior on $\mathbf{x}$, we need only revise $\mathbf{\Sigma}$ to be $(\mathbf{\Sigma_x}^{-1} + \mathbf{A}^{\mathrm{T}}\mathrm{Var}(\mathrm{p}(\mathbf{y}|\mathbf{x}))^{-1}\mathbf{A})^{-1}$.

3. Rim Reflectance Imaging

Under certain conditions, points observed near the occlusion boundaries of an object can be especially informative for reconstructing the incident lighting, even for objects with diffuse reflectance. Because the surface orientation of these points is almost perpendicular to the viewing direction, the lighting they reflect is restricted mainly to one side of the viewer (Fig. 2, red hemisphere).

We make the following simple observation: points near the rim strongly constrain the unknown incident lighting, provided that the lighting is limited to a compact range of directions separated from the viewing direction. In this setting, the intensity difference between adjacent points near the rim (Fig. 2, red and blue dots) may be attributed to a particular 1D oriented slice of the lighting. In theory, given high enough resolution and SNR, these 1D slices of incident lighting measured around the rim may be combined to resolve the lighting to any desired accuracy.

Although the conditions for rim reflectance imaging are limited (constrained lighting, high resolution and SNR, known geometry and albedo), we propose a new astronomy application with the necessary geometry. To our knowledge,

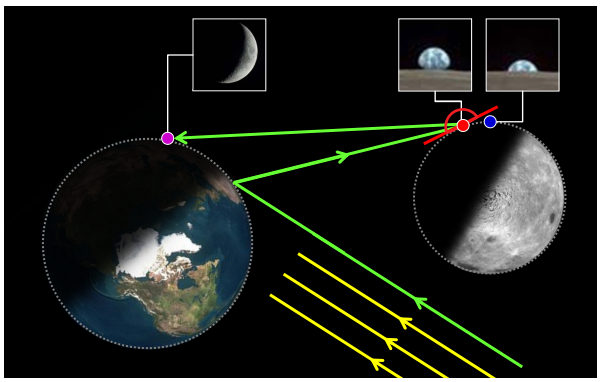

Figure 2: Rim reflectance imaging, demonstrated with the earth-moon system (not to scale), looking downward at the north pole. From a point on earth at night (magenta dot), we observe an image of the diffuse moon. The dark side of the lunar disk is lit exclusively by earthshine, *i.e.*, by sunlight reflected from earth, with an example light path shown in green. Due to occlusion geometry, points near the lunar rim (red and blue dots) reflect light from only a limited region of earth. Such points effectively experience "earthrise" (NASA Apollo 8 photos for illustration only), therefore the intensities of adjacent rim points constrain a 1D oriented slice of the lighting. In this context, rim reflectance can potentially let us recover an image of earth from space from a single ground-based photo of the moon.

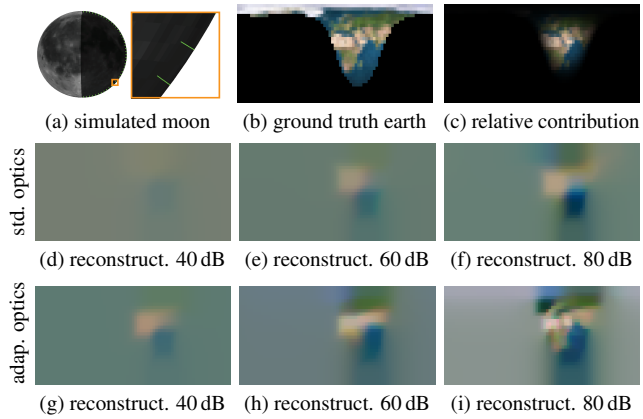

Figure 3: Single-shot earth reconstruction by rim reflectance imaging of the moon. We simulated the moon from Boston on August 3, 2010 at 2:00am, and considered 2475 points near the rim (green dots), distributed over 45 radial lines on the dark side of the disk (a). Only part of the earth, described by an RGB texture map, is visible to both the sun and moon (b), and some regions contribute more to the observed moon intensity (c). For various levels of measurement noise, expressed as PSNR, we show reconstructions using a sparse prior, and assuming a resolution of $0.4''$ (d-f). With a finer resolution of $0.07''$, corresponding to a large telescope with adaptive optics, our reconstructions recover much more detail (g-i).

intensity variations near occlusion boundaries have not previously been exploited to reconstruct incident lighting, and ours is the first method to enable diffuse reflectance imaging from a single shot.

3.1. Observing Earth in the Lunar Rim

For points near the dark edge of the lunar disk, the requirements of rim reflectance imaging are satisfied naturally (Fig. 2). Such points are lit only by earthshine, *i.e.*, by sunlight reflected from earth. Since the earth subtends less than 2° from the moon, the range of lighting directions is compact. Moreover, since we observe the moon at night, no light is reflected from the direction of the observer.

Rim reflectance imaging thus offers the promise of reconstructing an image of the earth as seen from space, from a *single* earth-bound photo of the moon. We studied the feasibility of this approach with detailed simulations, and conclude that interesting earth structure could potentially be resolved (Fig. 3). As our results show, this approach is limited mainly by the resolution of ground-based astronomy.

To take advantage of the quickly varying visibility near the rim, it is crucial to capture high-resolution images of the moon. For ground-based astronomy, resolution is generally limited by the turbulence of the atmosphere rather than the optics. We tested our reconstruction method under two resolutions. First, we assumed a resolution of $0.4''$ (Fig. 3def), corresponding to ideal atmospheric conditions [11], but without the order-of-magnitude improvement offered by adaptive optics [6]. Second, we assumed a more optimistic resolution of $0.07''$ (Fig. 3ghi), corresponding to moon images previously captured using an 8 m ground-based telescope with adaptive optics [6]. Since the moon has an average diameter of 0.5°, these resolutions correspond to 4 500 and 26 000 pixels across the lunar disk respectively.

To put the noise levels in Fig. 3 in context, sensors used in astronomy (*e.g.*, the Kodak KAF-4320) can have PSNRs of more than 80 dB. Given other sources of uncertainty, the 80 dB level is meant to represent an optimistic but not impractical SNR. The other levels shown, 40 dB and 60 dB, represent moderate and high-quality imaging respectively.

Geometry and sampling Existing astronomical models for earth, moon, and sun provide us with shapes, positions and orientations over time, known collectively as ephemeris [11]. Their accuracy is better than sufficient for reflectance imaging applications.

We discretized the surface of the earth into 75×30 pixels using a latitude-longitude projection. To correct for nonuniformity we incorporate a weighting in our prior model inversely proportional to pixel area, so that regions near the poles are penalized more for non-smoothness.

We selected samples near the rim of the moon along 45 evenly spaced radial lines (Fig. 3a). Each line contained 55 points, from the dark rim inwards, spaced according to the assumed resolution. Increasing the number of samples did not qualitatively affect the results, apart from the effective denoising due to having more observations.

Reflectance models In our simulations we used a detailed model of moon reflectance described by Hapke [5], including

physically-based retroreflectance and scattering. This model explains the well-known opposition effect, that the full moon appears uniformly bright across the disk, versus the darkened rim expected for a Lambertian sphere. In practice, Hapke is not much easier to invert than Lambertian reflectance, since earthshine covers a small range of directions.

We modeled the earth as a Lambertian reflector. Although this is a major simplification, as a whole the earth is roughly Lambertian over phases of interest [14]. While land forms, oceans, and clouds all reflect light differently [23, 14, 24], our Lambertian assumption removes the need to introduce *a priori* knowledge about the map we are trying to reconstruct. The earth albedos we recover using this approach should thus be treated as a more qualitative snapshot, modulated by the true spatially-varying reflectance.

Discussion For the purposes of our feasibility study, we have ignored the complications of both spatially-varying lunar albedo and of topography near the lunar rim that could affect visibility. Such information, however, can be recovered by other means, even if we restrict ourselves to earth-bound measurements. For example, the full moon image provides a rough estimate of albedo, and detailed topography near the rim could be resolved by observing the moon's silhouette as it librates (*i.e.*, appears to wobble). Furthermore, we can be selective about which moon pixels to sample, avoiding regions with greater albedo or topography variation.

To put this method into practice, we would need to take a careful approach to imaging. Two important considerations are blocking the glare from the bright side of the lunar disk [15] and tracking the moon to avoid motion blur over the long exposures required for high-SNR earthshine measurements.

4. Time-Varying Reflectance Imaging

If the diffuse reflector changes over time, capturing multiple photos can provide another useful source of variation for recovering structure. For example, if a diffuse reflector is rotated on a turntable, its changing occlusion geometry can help us better resolve the incident lighting.

In astronomical imaging, time-varying reflectance arises naturally, since the relative position of the bodies we observe change over time, as both the observer and target move along their respective orbits (Fig. 4). For distant planets like Pluto [28] or extra-solar planets, the only "images" we can resolve are extremely low-resolution—as low as a single pixel—so temporal variation provides the only data available, leading to an extreme but highly structured super-resolution problem.

Astronomers refer to photometric measurements over time as *light curves*, and the reconstruction of planetary surface albedo from light curves is a classic problem originally posed over a century ago [20]. While light curves have historically been used in a more qualitative way, *e.g.*, to provide evidence of large scale non-uniformities in surface albedo. recent methods have sought more detailed reconstructions

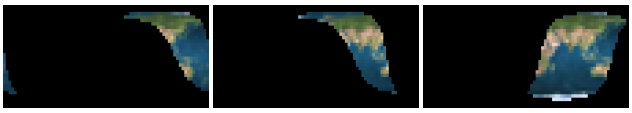

(a) 1am, Feb 24, 2010 (b) 5am, Feb 24, 2010 (c) 2am, Aug 14, 2010

Figure 4: Region of the earth visible at different times from the moon's disk. Over a given night, the rotation of the earth effectively scans this region westward (a,b). The orientation of the region varies over season (c), and its width varies with lunar phase. See Fig. 3b as well.

[26, 28] using the same linear formulation as we do. In this setting, our technical contribution is the Bayesian analysis and our generalization handling time-varying surface albedo as well (Sec. 2.2).

4.1. Earth from a Single-Pixel Moon

Over time, the geometry of the earth-moon system (Fig. 2) evolves as the bodies move in their orbits. In theory, we can take advantage of these variations, using earthshine reflected in the moon to scan over different illuminated regions of earth (Fig. 4) and building up a composite "long-exposure" photograph of the earth from space. Compared to our single-shot approach (Sec. 3.1), exploiting variations over time has the benefits that low spatial resolution is sufficient and we can obtain nearly full coverage of the globe.

Each day, as the earth completes a revolution on its axis, it sweeps from east to west the region of earth that is illuminated and visible to the moon (Fig. 4ab). Furthermore, the moon orbits the earth roughly every 28 days, passing through different phases relative to the sun. These phases describe what fraction of the lunar disk is illuminated by the sun, and correspondingly, what fraction of the earth reflects light toward the moon (Fig. 4). Although the moon only sweeps out a 1D orbit around the earth, the passage of time can provide richer geometric variation than the 1D sweep achievable in a 24-hour period. In particular, the 23° axial tilt of the earth relative to its orbital plane (giving rise to the seasons), combined with the 5° relative incline of the moon's orbital plane, provides additional variation in the direction perpendicular to the earth's orbit (Fig. 4c).

In an ongoing project, the time-varying intensity of earthshine has been systematically observed for more than 10 years, for the purpose of monitoring changes in overall albedo of the earth [15, 14]. This project effectively seeks *single-pixel* reconstructions of the earth from its reflection in the moon. By contrast, we are interested in evaluating the feasibility of combining such measurements to resolve greater surface detail on the earth.

Cloud-free reconstruction To investigate the feasibility of such data for surface reconstruction, we first present best-case results with the simplifying assumption that the appearance of the earth does not vary over time. This ignores the main challenge of reconstructing the earth from time-

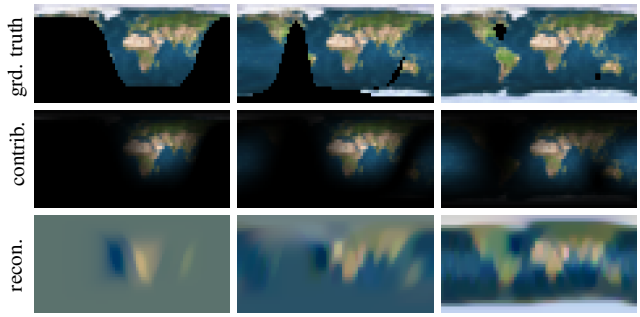

(a) 1 night
Aug 12–13, 2010
107 obs. (3 min)

(b) 1 month
Aug 2010
412 obs. (10 min)

(c) 1 year
Jan-Dec 2010
963 obs. (60 min)

Figure 5: Reconstructions of cloud-free earth from simulated single-pixel moon observations over different timespans, using a sparse prior and assuming a PSNR of 60dB. For each timespan, the sampling rate is shown in brackets. The observer is simulated to be in Boston, and since we only capture moon photos at night, the surrounding area is always dark. As a result, the western hemisphere contributes less to the reflected moon intensity (top, middle row) and its reconstruction is relatively worse (bottom row).

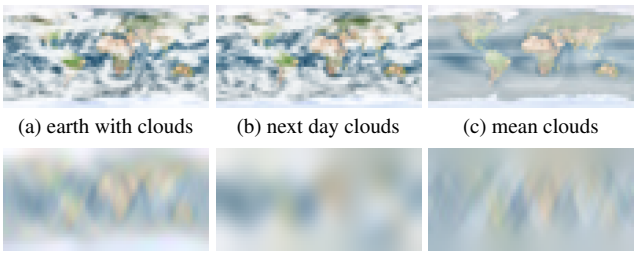

(a) earth with clouds (b) next day clouds (c) mean clouds

(d) baseline (e) basic recon. (f) covariant recon.

Figure 6: Reconstruction of earth with time-varying clouds, with clouds given by daily ISCCP satellite data [7] (a-c). We simulated single-pixel moon observations over a year at 3 min intervals, assuming a PSNR of 60 dB. To define a baseline (d), we reconstruct the earth from observations assuming a fixed albedo map set to the ground truth earth with mean cloud cover (c). When our observations are modified to take into account time-varying clouds, our basic reconstruction method treats these variations as i.i.d. noise and fails to recover detailed structure (e). However, using our block-wise marginalization of the daily clouds (f), we can achieve results much closer to the baseline.

varying measurements, namely its highly-varying surface appearance over time. Such variation is due mainly to changing cloud cover (over the timescale of hours and days), but also variations in vegetation and snow (over the seasons).

As our cloud-free results show, significant earth structure can be reconstructed from observations over a month or longer, and a year of observations allows us to recover greater resolution still (Fig. 5). More detailed investigation confirmed that the higher quality of reconstructions from year-long measurements is due to the greater variation in occlusion geometry.

Note the relatively poor resolution of the Americas in our reconstructions. Since the simulated observer is in Boston and we are constrained to observe the moon at night, the observer receives almost no earthshine from this part of the earth. Even over longer observation periods, North America is still relatively low resolution (Fig. 5c); the observer can never measure earthshine from himself or his antipode.

Modeling cloud variations Next, we explored the effect of time-varying clouds, using our more sophisticated reconstruction method (Sec. 2.2) to marginalize out the per-night variations in cloud cover. This approach lets us explain away the changing cloud cover as covariant noise, and obtain a reasonable reconstruction of the stable earth appearance, *i.e.*, the earth with mean cloud cover (Fig. 6).

We used daily cloud cover measurements taken from the satellite-based ISCCP dataset [7], telling us that about 64% of the earth is covered by clouds on average, and that the bulk of the light reflected from earth is due to relatively high-albedo clouds. At the resolution that we hope to reconstruct the earth albedo, it is reasonable to consider clouds as constant within each nighttime moon observation period (between 1–5 hours). Continent-sized cloud formations have an typical lifespan of 3 days.

Simulation parameters We followed the same procedures described earlier (Sec. 3.1), computing the geometry from detailed astronomical ephemeris [11] and using the same moon and earth reflectance models. To obtain a single brightness measurement from the moon, we sampled a set of 10 points with fixed lunar coordinates [15], and averaged the intensities of those points lying on the earthshine side.

We simulated moon photos only at times when such photos were plausible. In particular, we require that the moon is at least 2° above the horizon; that the sun is at least 8° below the horizon, to limit twilight glare; and that the lunar disk is below 85% full, to limit glare from the moon.

4.2. Mars from Single-Pixel Observations

We also tested our time-varying reconstruction method using single-pixel observations of Mars to reconstruct the Martian surface. This application can be thought of as a feasibility test for reconstructing more distant planets, but in a controlled situation where ground truth is known. In the context of direct planetary observation, both geometry and lighting are known (*i.e.*, from ephemeris) and we seek to recover the unknown surface albedo.

Since Mars is exterior to the earth's orbit, it is always observed as near full, with at least 85% of the Martian disk lit by the sun. As a result, although we can take advantage of temporal variation as Mars spins on its axis, visibility geometry only provides limited assistance in reconstructing the surface, since single-pixel observations of always involve a large fraction of the Martian area.

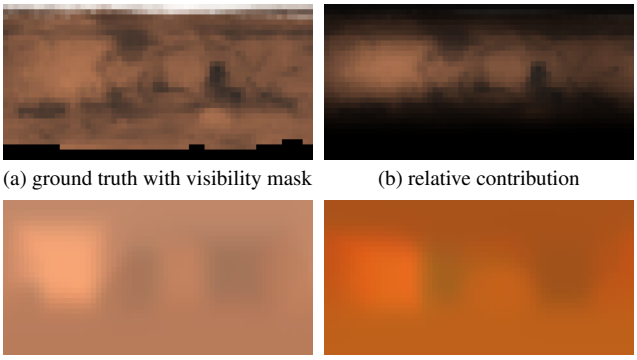

(a) ground truth with visibility mask (b) relative contribution

(c) recon. from simulation, rescaled (d) recon. from real data, hVB bands

Figure 7: Reconstruction of the Martian surface from 234 single-pixel spectra measured from 1963–1965 [8, 9]. By exploiting the time-varying occlusion geometry, we recovered a coarse hyperspectral map of Mars, with a spatial resolution of roughly 6×1, shown in false color (d). Given the limited number of measurements, their moderate 47 dB PSNR, and the limited phase variation of Mars, our method performs as well as expected. Resolution at the poles is poor, because the Martian south pole is not visible in these measurements (a) and most light is reflected from near the equator (b). To evaluate our reconstruction, we used a ground truth visible-wavelength map of Mars (a) to simulate single-pixel observations under the same conditions as the real data. Reconstructions from these simulations (c) agree qualitatively, validating our real reconstructions and demonstrating the intrinsic difficulty of the inverse problem.

Reflectance model In contrast with more detailed spectral models of Martian reflectance available [25], we adopt a simple model proposed for shape-from-shading from images of Mars [2], the empirical Minnaert BRDF, $\rho(\vec{\omega}_i, \vec{\omega}_o) = \frac{1}{\pi}\left((\vec{\omega}_i \cdot \vec{n})(\vec{\omega}_o \cdot \vec{n})\right)^{k-1}$ with $k = 0.72$.

Real planetary photometry data To test the capability of our reconstruction method, we considered a set of single-pixel photometry measurements made of Mars between 1963–1965 [8, 9]. Although these data were not collected to recover surface detail, nor have they been previously analyzed in this way, we show that these historical measurements indeed encode coarse surface structure (Fig. 7).

The Martian photometry data we used was collected from observatories in South Africa and France. In total, the data consists of 234 single-pixel measurements of Mars over 13 spectral bands, but with significant missing data. We entered the tabulated data by hand then made adjustments to account for varying data collection and record-keeping procedures [27]. The photometry measurements were performed carefully, cooling the detector to reduce noise, and correcting for airmass using calibration against a standard set of stars. Still, the data is given to relatively low precision, with 0.9% relative error at best. We set the noise level of our model to match this error, corresponding to a PSNR of 47 dB.

To visualize our reconstruction results, we generated false color images (Fig. 7d) from three spectral bands. In particular, we used the narrow-band filter at 730 nm (h) and two standard astronomy filters in green and blue (V, B).

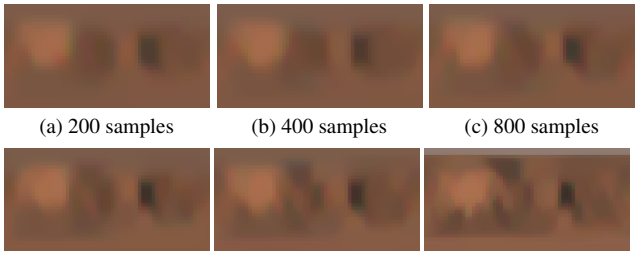

(a) 200 samples (b) 400 samples (c) 800 samples

(d) 1600 samples (e) 3200 samples (f) 23731 samples

Figure 8: Reconstructions of Mars from varying numbers of simulated observations, using a sparse prior and assuming a PSNR of 60 dB. All observations were simulated over the same 2-year period (about 1 Martian year), with observation times sampled randomly (a-e) or spread uniformly (f) over all plausible times for Mars photography. Results represent best-case reconstructions, since temporal surface variations (*e.g.*, clouds) were not considered.

Simulation study To explore for the limits of the reconstruction of Mars, we simulated capturing more observations with higher PSNR (Fig. 8), assuming optimistically that the surface albedo of Mars remains constant over time. Although Mars does experience weather, its cloud formations are smaller and more stable than those on earth. Compared to our time-varying reconstructions of earth (Figs. 5–6), our Mars results are lower resolution, mainly because exterior planets like Mars provide less natural variation over time from their occlusion geometry.

5. Discussion

Although geometry was known for all our applications, given a previously unseen target, we may not have the opportunity to measure its geometry directly. In such cases, diffuse reflectance imaging is a blind problem, where both the lighting and the transfer matrix must be resolved.

For distant planets, not knowing the orbital parameters *a priori* may not be a limiting factor; parameters such as orientation and rotation rate may be inferred by analyzing periodic structure in the light curves [13]. Unknown geometry presents more of a challenge for asteroids [20], whose irregular 3D shapes can lead to complicated tumbling. Even assuming constant albedo, recovering 3D shape from light curves is a highly ill-posed problem.

It is also an interesting question to what extent the BRDF itself can be recovered from diffuse reflectance [19], particularly if BRDF is allowed to vary spatially over the object. Intuitively, this seems like a very challenging problem, even if BRDF can be described with a limited parameterization.

6. Conclusions

As we showed, occlusion geometry is a crucial consideration when measuring reflectance using diffuse objects. We

demonstrated the value of occlusion in both theoretical and practical terms, and proposed a new reconstruction method that takes advantage of occlusion at object boundaries. We investigated several astronomy applications that fit naturally into this framework. Among other results, we showed two ways in which it may be feasible to reconstruct an image of the earth from space using only ground-based observations of the earth's reflection in the moon.

We are currently analyzing real earthshine data [15, 14] in an effort to further validate our reconstruction methods. For future work, we are interested in taking advantage of geometric complexity and temporal variation for imaging in everyday settings. Our hope is to uncover new imaging abilities in the scene itself, expanding our notion of a camera.

Acknowledgments We would like to thank Bernhard Schölkopf and Frédo Durand for helpful discussions, Livia Ilie for early participation as an MIT UROP, and David Chen for help with data entry. This work was supported in part by an NSERC Postdoctoral Fellowship, BSF Grant 2008155, NGA NEGI-1582-04-0004, MURI Grant N00014-06-1-0734, the ISF, ERC, and Quanta T-Party, and gifts from Microsoft, Google and Adobe.

References

[1] R. Basri and D. W. Jacobs. Lambertian reflectance and linear subspaces. *TPAMI*, 25:218–233, Feb. 2003. 1, 2

[2] R. A. Beyer, A. S. McEwen, and R. L. Kirk. Meter-scale slopes of candidate MER landing sites from point photoclinometry. *J. Geophys. Research*, 108(E12):8085, 2003. 7

[3] C. M. Bishop. *Pattern Recognition and Machine Learning*. Springer-Verlag, 2006. 3

[4] F. Durand, N. Holzschuch, C. Soler, E. Chan, and F. X. Sillion. A frequency analysis of light transport. In *SIGGRAPH*, pp. 1115–1126, 2005. 2

[5] B. Hapke. Bidirectional reflectance spectroscopy: 4. the extinction coefficient and the opposition effect. *Icarus*, 67(2):264–280, 1986. 4

[6] J. Hewett. Adaptive optics focus on the moon, http://optics.org/article/9654/, Aug. 2002. 4

[7] International Satellite Cloud Climatology Project (ISCCP). http://isccp.giss.nasa.gov/. 6

[8] W. M. Irvine, T. Simon, D. H. Menzel, J. Charon, G. Leconte, P. Griboval, and A. T. Young. Multicolor photoelectric photometry of the brighter planets. II. Observations from Le Houga Observatory. *Astronom. J.*, 73:251–264, May 1968. 7

[9] W. M. Irvine, T. Simon, D. H. Menzel, C. Pikoos, and A. T. Young. Multicolor Photoelectric Photometry of the Brighter Planets. III. Observations from Boyden Observatory. *Astronom. J.*, 73:807–828, Nov. 1968. 7

[10] A. Levin, R. Fergus, F. Durand, and W. T. Freeman. Image and depth from a conventional camera with a coded aperture. In *SIGGRAPH*, 2007. 1, 3

[11] O. Montenbruck and T. Pfleger. *Astronomy on the Personal Computer*. Springer-Verlag New York, 4th edition, 2000. 4, 6

[12] K. Nishino and S. K. Nayar. Eyes for relighting. In *SIGGRAPH*, pp. 704–711, 2004. 1

[13] E. Pallé, E. B. Ford, S. Seager, P. Montañés-Rodríguez, and M. Vazquez. Identifying the rotation rate and presence of dynamic weather on extrasolar earth-like planets from photometric observations. *Astrophys. J.*, 676(2):1319, 2008. 7

[14] E. Pallé, P. R. Goode, V. Yurchyshyn, J. Qiu, J. Hickey, P. Montañés Rodriguez, M. Chu, E. Kolbe, C. T. Brown, and S. E. Koonin. Earthshine and the Earth's albedo: 2. Observations and simulations over 3 years. *J. Geophys. Research*, 108:4710, Nov. 2003. 5, 8

[15] J. Qiu, P. R. Goode, E. Pallé, V. Yurchyshyn, J. Hickey, P. Montañés Rodriguez, M. Chu, E. Kolbe, C. T. Brown, and S. E. Koonin. Earthshine and the Earth's albedo: 1. Earthshine observations and measurements of the lunar phase function for accurate measurements of the Earth's Bond albedo. *J. Geophys. Research*, 108:4709, Nov. 2003. 5, 6, 8

[16] R. Ramamoorthi and P. Hanrahan. On the relationship between radiance and irradiance: determining the illumination from images of a convex Lambertian object. *JOSA A*, 18(10):2448–2459, Oct. 2001. 1, 2

[17] R. Ramamoorthi and P. Hanrahan. A signal-processing framework for inverse rendering. In *SIGGRAPH*, pp. 117–128, 2001. 1, 2

[18] R. Ramamoorthi and P. Hanrahan. A signal-processing framework for reflection. *ACM Trans. Graph.*, 23:1004–1042, Oct. 2004. 1, 2

[19] F. Romeiro and T. Zickler. Blind reflectometry. In *ECCV*, vol. 1, pp. 45–58, 2010. 7

[20] H. N. Russell. On the light variations of asteroids and satellites. *Astrophysical J.*, 24:1–18, July 1906. 1, 5, 7

[21] S. M. Seitz, Y. Matsushita, and K. N. Kutulakos. A theory of inverse light transport. In *ICCV*, pp. 1440–1447, 2005. 1, 2, 3

[22] P. Sen, B. Chen, G. Garg, S. R. Marschner, M. Horowitz, M. Levoy, and H. P. A. Lensch. Dual photography. In *SIGGRAPH*, pp. 745–755, 2005. 1, 2, 3

[23] J. T. Suttles, R. N. Green, P. Minnis, G. L. Smith, W. F. Staylor, B. A. Wielicki, I. J. Walker, D. F. Young, V. R. Taylor, and L. L. Stowe. *Angular radiation models for earth-atmosphere system. Volume I, Shortwave radiation*. NASA Ref. Publ. 1184, Washington DC, 1988. 5

[24] G. Tinetti, V. S. Meadows, D. Crisp, W. Fong, E. Fishbein, M. Turnbull, and J. Bibring. Detectability of Planetary Characteristics in Disk-Averaged Spectra. I: The Earth Model. *Astrobiology*, 6:34–47, Mar. 2006. 5

[25] G. Tinetti, V. S. Meadows, D. Crisp, W. Fong, T. Velusamy, and H. Snively. Disk-averaged synthetic spectra of mars. *Astrobiology*, 5(4):461–482, 2005. 7

[26] W. J. Wild. Matrix formalism for inferring planetary surface albedo distributions from light-curve measurements. *Astronomical Society of the Pacific, Publications*, 101:844–848, Sept. 1989. 1, 5

[27] A. T. Young and W. M. Irvine. Multicolor photoelectric photometry of the brighter planets. I. Program and Procedure. *Astronom. J.*, 72:945–950, Oct. 1967. 7

[28] E. F. Young, K. Galdamez, M. W. Buie, R. P. Binzel, and D. J. Tholen. Mapping the Variegated Surface of Pluto. *Astronom. J.*, 117:1063–1076, Feb. 1999. 1, 5

[29] A. Zomet and S. K. Nayar. Lensless imaging with a controllable aperture. In *CVPR*, vol. 1, pp. 339–346, 2006. 1